

Article

Graded Grain Structure to Improve Hydrogen-Embrittlement Resistance of TWIP Steel

Seok Weon Song ¹, Taekyung Lee ^{2,*}  and Chong Soo Lee ^{3,*} ¹ Technical Research Laboratories, POSCO, Pohang 37877, Korea; ssw623@posco.com² School of Mechanical Engineering, Pusan National University, Busan 46241, Korea³ Graduate Institute of Ferrous Technology, Pohang University of Science and Technology (POSTECH), Pohang 37673, Korea

* Correspondence: taeklee@pnu.ac.kr (T.L.); cslee@postech.ac.kr (C.S.L.)

Received: 22 October 2020; Accepted: 16 November 2020; Published: 17 November 2020



Abstract: The high strength of twinning-induced plasticity (TWIP) steels makes them vulnerable to the hydrogen embrittlement (HE) phenomenon, thereby limiting their potential applications. This study suggests inducing a graded grain structure (GGS) in a Fe-17Mn-0.8C TWIP steel through shot peening and subsequent heat treatment to solve the problem. The microstructures and fracture surfaces of GGS TWIP steel were compared with those of conventionally manufactured TWIP steel possessing a uniform grain structure (UGS). Compared with the conventional UGS TWIP steel, GGS steel showed similar tensile properties with a yield strength of 310 MPa, tensile strength of 1060 MPa, and elongation-to-failure of 135%. It also exhibited moderately enhanced low-cycle fatigue (LCF) resistance in terms of fatigue life (8196 cycles to failure) compared with the UGS steel (7201 cycles). Furthermore, GGS TWIP steel exhibited a marked improvement in HE resistance, both in the monotonic (by a slow-strain-rate test) and cyclic deformation modes (by the LCF test) in a hydrogen environment. A relatively fine-grained ($d = 15.6 \mu\text{m}$) surficial area enhanced the HE resistance by inhibiting hydrogen penetration and decreasing twin density, while the coarse-grained ($d = 74.6 \mu\text{m}$) interior promoted the LCF resistance by suppressing crack growth.

Keywords: graded; hydrogen embrittlement; tensile; fatigue; TWIP steel

1. Introduction

Twinning-induced plasticity (TWIP) steel has been considered as one of most promising structural materials by various industries. Such a reputation arises from remarkable mechanical properties of this steel. For example, the strength–ductility balance of TWIP steels deviates from the trade-off relationship made by traditional ferrous alloys including dual-phase, high-strength and low-alloy, bake-hardening, extra-mild, and complex-phase steels [1]. TWIP steels also exhibit an excellent capability of strain hardening due to the formation of mechanical twinning during a plastic deformation [2]. Nevertheless, several material issues have yet to be overcome for the wider application of TWIP steels, such as a low yield strength (YS), relatively poor wet corrosion resistance, and susceptibility to hydrogen embrittlement (HE) [3].

Among these issues, HE refers to the degradation of mechanical properties owing to hydrogen dissolved in a lattice structure [4]. The high strength of TWIP steels makes them vulnerable to the HE phenomenon, thereby limiting their potential applications [5]. Researchers have suggested various strategies to increase the HE resistance of TWIP steels, which can be roughly classified into two categories: the addition of particular alloying elements (e.g., Al, Cu, and V) [6–11] and grain refinement [12,13]; this study focused on the latter approach. Although grain refinement is an effective way to improve HE resistance, a fine-grained microstructure brings about the acceleration of fatigue

crack growth and deterioration in a low-cycle fatigue (LCF) life [14,15]. This makes it difficult to adopt the approach of grain refinement in industries that require HE resistance in monotonic and cyclic deformation modes simultaneously, such as gas vessels and pipes. Furthermore, grain refinement of a bulk material is often impractical owing to the expensive and complicated processes as well as limited material dimensions. For example, most severe plastic deformation processes (e.g., equal-channel angular pressing and high-pressure torsion) are inapplicable to mass production due to their intrinsic non-continuous manufacturing procedure [16]. Fine- or ultrafine-grained metals fabricated by these methods have a significantly limited dimension of a few centimeters as well [17].

As an alternative approach, the present study suggests exploiting a graded grain structure (GGS) to enhance the HE resistance of TWIP steel in both deformation modes. Fe-17Mn-0.8C steel was chosen to verify this idea, as massive amounts of background data, particularly with respect to HE [7,8,18], were expected to assist in interpreting the results obtained in this work. The logical basis for the present strategy is the fact that hydrogen cannot penetrate deeply into the face-centered cubic (FCC) structure, which leads to a high hydrogen concentration at a surface layer of the material [7,8]. Accordingly, grain refinement was induced only at the surface layer in this strategy, while leaving the interior microstructure relatively unchanged. The HE resistance of the developed GGS steel has been discussed in terms of its microstructure as compared to a conventional steel with a uniform grain structure (UGS).

2. Materials and Methods

An austenitic TWIP steel was produced by vacuum induction melting, of which the chemical composition is Fe-17.0Mn-0.80C-0.21Si-0.22Cr-0.20Ni-0.02N- < 0.02P- < 0.001S (numbers in mass percentage). The cast ingot was solution treated at 1473 K and hot-rolled into plates with a thickness of 15 mm, followed by heat treatment at 1373 K for 1 h. The steel manufactured by such a conventional procedure has been referred to UGS steel hereafter. The GGS steel was fabricated by applying a shot-peening process to UGS steel. The process was performed in all directions of the sample, using 0.4-mm metallic balls for 8 min under a pressure of 20 MPa, followed by annealing at 1123 K for 3 min.

Hydrogen was electrochemically charged into the investigated steels at a current density of $30 \text{ A}\cdot\text{m}^{-2}$ in an aqueous solution of 3% NaCl and 0.3% NH_4SCN . The charging temperature and time varied in ranges of 298–360 K and 6–24 h, respectively. Sections of these specimens were directly subjected to thermal desorption analysis (TDA); they were heated up to 1000 K at a heating rate of $100 \text{ K}\cdot\text{h}^{-1}$, during which the released hydrogen gas was transferred to a gas chromatograph per 4 min. The other sections were Zn-coated immediately after the hydrogen charging to prevent the internal hydrogen from diffusing out during the mechanical tests introduced below.

Grain structure was investigated by electron backscatter diffraction (EBSD) analysis. The EBSD samples were mechanically ground with #400- to #2400-grit SiC paper, and then electro-polished at 45 V in a solution of 95% acetic acid and 5% perchloric acid. The EBSD analysis was performed at a step size of $0.5 \mu\text{m}$. The data with a high (≥ 0.1) confidence index were processed using TSL OIM Ver. 7 software. The fracture surface was characterized using scanning electron microscopy (SEM) at 15 kV.

The slow-strain-rate test (SSRT) and LCF test were employed to investigate the mechanical properties in the monotonic and cyclic deformation modes, respectively. For both tests, the loading direction was aligned with the rolling direction of the initial hot-rolled plate. The SSRT was conducted at an initial strain rate of $5 \times 10^{-5} \text{ s}^{-1}$ using a plate-type specimen of 25 mm in gage length, 6 mm in gage width, and 3 mm in gage thickness. The LCF test was performed with similar plate-type specimens with a gage length of 7.5 mm. The strain-controlled test adopted a triangular waveform with a frequency of 1 Hz and a fixed strain amplitude of 5×10^{-3} .

3. Results and Discussion

The investigated materials showed different grain characteristics (Figure 1). The microstructure of GGS steel varied significantly depending on the location. The surface layer consisted of grains with an average size of $15.6 \mu\text{m}$. This relatively fine-grained area lay approximately $60 \mu\text{m}$ deep below the

surface, which accounted for 6% of the volume fraction. In contrast, the interior showed remarkably coarser (74.6 μm) grains with an equiaxed morphology. UGS steel was composed of uniformly coarse (76.3 μm) grains, of which the size was similar to that of the interior of GGS steel.

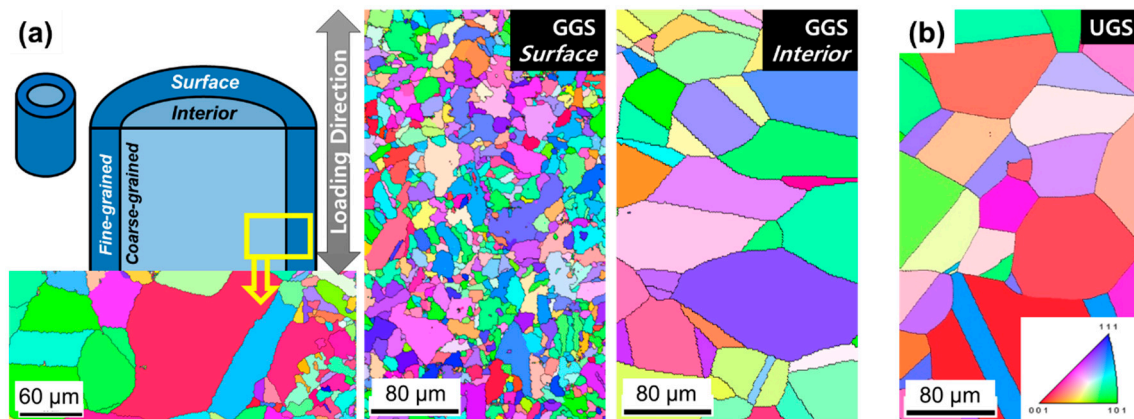


Figure 1. Electron backscatter diffraction (EBSD) inverse pole figure map of (a) GGS and (b) UGS TWIP steels. The images are perpendicular to the normal direction.

Before hydrogen charging, both samples exhibited comparable mechanical properties in the monotonic deformation mode (i.e., SSRT). GGS steel exhibited YS of 310 MPa, an ultimate tensile strength (UTS) of 1060 MPa, and elongation-to-failure (EL) of 135%. UGS steel showed slightly lower strengths (YS of 295 MPa and UTS of 1040 MPa) but higher ductility (EL of 140%). The YS is governed by the Hall–Petch relation: $YS = \sigma_0 + k^{H-P}/\sqrt{d}$ where σ_0 is the friction stress, k^{H-P} is a constant, and d is a grain size [19]. Applying the rule of mixtures, the Hall–Petch relation yielded a negligible difference in the YS values (<10 MPa) between GGS and UGS steels because of the low fraction of fine-grained area in the former. This calculated result was in good agreement with the experimental data.

Meanwhile, in the cyclic deformation mode, GGS steel showed 14% enhanced LCF life (8196 cycles to failure) as compared to that of the UGS sample (7201 cycles). These results are consistent with those reported in a previous study [20]. The authors attributed the improved LCF properties to the inhibition of crack initiation by the relatively fine-grained area, prevailing geometrically necessary dislocations, and relaxed surface stress because of a core-shell structure.

The hydrogen charging gave rise to a significant change in the mechanical properties (Figure 2). According to previous studies, hydrogen released at temperature lower than 600 K corresponds to diffusible hydrogen trapped at either dislocations or grain boundaries in TWIP steels [9]. This type of hydrogen diffuses inside a steel due to its relatively low activation energy (<20 $\text{kJ}\cdot\text{mol}^{-1}$) [4]. Both types of steel showed a loss in ductility with an increasing amount of diffusible hydrogen in the monotonic deformation mode. However, the extent of deterioration was obviously reduced in GGS steel, as is clearly confirmed by the arrows in Figure 2a; the loss of EL was 6.3% for GGS steel and 23.3% for UGS steel under the same hydrogen-charging conditions. Similar results were confirmed in the cyclic deformation mode. For example, the loss of LCF life was 12% for GGS steel in contrast to 53% for UGS steel under the same condition marked by the dotted circles in Figure 2c. The number of cycles to failure for UGS steel rapidly decreased, with even a low amount of diffusible hydrogen (<2 mass ppm) resulting in a significant deterioration in LCF life as compared to GGS steel. It is thus concluded that GGS steel exhibited an enhanced HE resistance both in the monotonic and cyclic deformation modes.

The SEM micrographs revealed the transition of fracture behavior owing to diffusible hydrogen (Figure 3). Hydrogen-uncharged TWIP steels showed the dimple fracture behavior in the monotonic deformation mode, regardless of the grain structure. In the cyclic deformation mode, these steels demonstrated fatigue crack initiation at the surface, as reported elsewhere [7]. In contrast, the hydrogen-charged steels presented a mixed microstructure of intergranular fracture at the surface layer and dimple fracture in the interior.

It should be noted that the size of the intergranular facet in GGS steel was notably finer than that in UGS steel, as marked by the red arrows in Figure 3c,d. Fatigue cracks were initiated at intergranular cracking sites in the subsurface area after the hydrogen charging, as marked by the yellow arrows in Figure 3g,h.

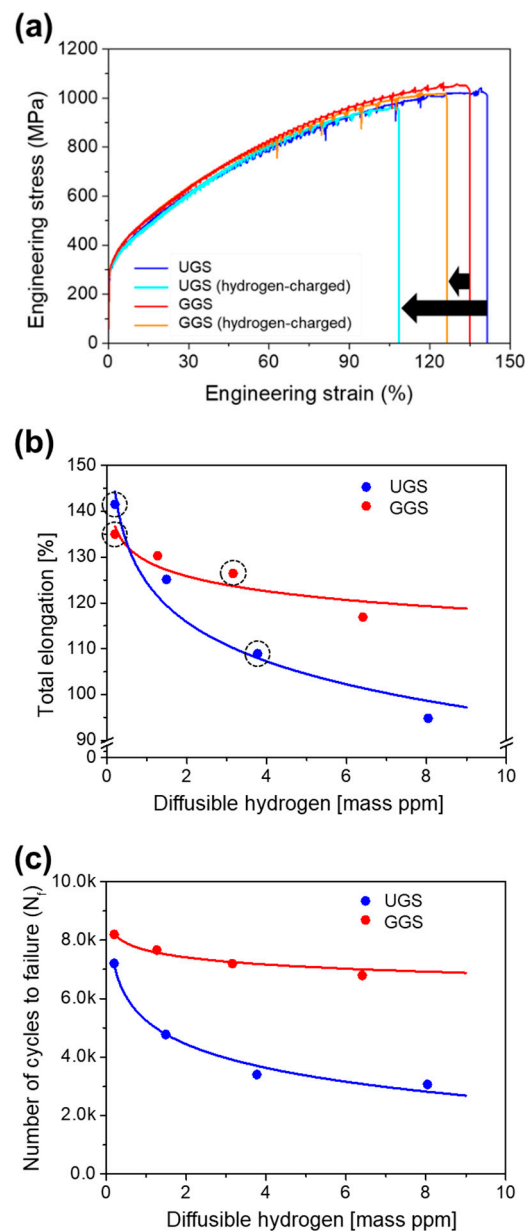


Figure 2. Variation in mechanical behaviors after hydrogen charging in the (a,b) monotonic and (c) cyclic deformation modes. Engineering stress–strain curves in Figure 2a correspond to the data points marked by the dotted circles in Figure 2b. In Figure 2a, hydrogen was charged at a current density of $30 \text{ A}\cdot\text{m}^{-2}$ for 6 h at 360 K.

The presence of diffusible hydrogen leads to reduced bonding energy of the grain boundaries and eventually causes intergranular fracture [8]. The intergranular fracture in the hydrogen-charged samples indicates the concentration of diffusible hydrogen near the surface layer. The extremely low diffusivity of hydrogen in the FCC structure hinders its penetration into TWIP steel [21]. Accordingly, the intergranular-fractured region can be recognized as a hydrogen-affected zone. It is worth noting that these zones were significantly narrow; they lay approximately 50 and 90 μm deep below the surface in the GGS and UGS steels, respectively. Hence, the relatively fine-grained area in GGS steel

(i.e., approximately 60 μm deep below the surface) was wide enough to cover the hydrogen-affected zone despite its low volume fraction.

Both steels exhibited TDA peaks at similar temperatures less than 600 K, regardless of the grain structure (Figure 4). These peaks correspond to the diffusible hydrogen trapped at grain boundaries and dislocations, as mentioned earlier, suggestive of the same type of hydrogen-trapping sites in GGS and UGS steels. The relevant area of the TDA spectrum of GGS steel was lower than that of UGS steel, resulting in 20% less diffusible hydrogen (3.7 mass ppm) than its counterpart (4.6 mass ppm). This result was also consistent with the lower fraction of the hydrogen-affected zone in the GGS steel. An active hydrogen trapping caused by grain refinement decreased the effective diffusivity coefficient during the electrochemical permeation of hydrogen [22], suggesting that the grain boundaries acted as a barrier to hydrogen penetration. This mechanism explains the inhibited hydrogen penetration by the relatively fine-grained surface layer in GGS steel, which resulted in a lower amount of diffusible hydrogen and improvement in HE resistance. Apart from this effect, it is noted that mechanical twinning was suppressed in the fine-grained area. The reduced density of hydrogen-enriched twin boundaries and junctions further contributed to the enhanced HE sensitivity [13].

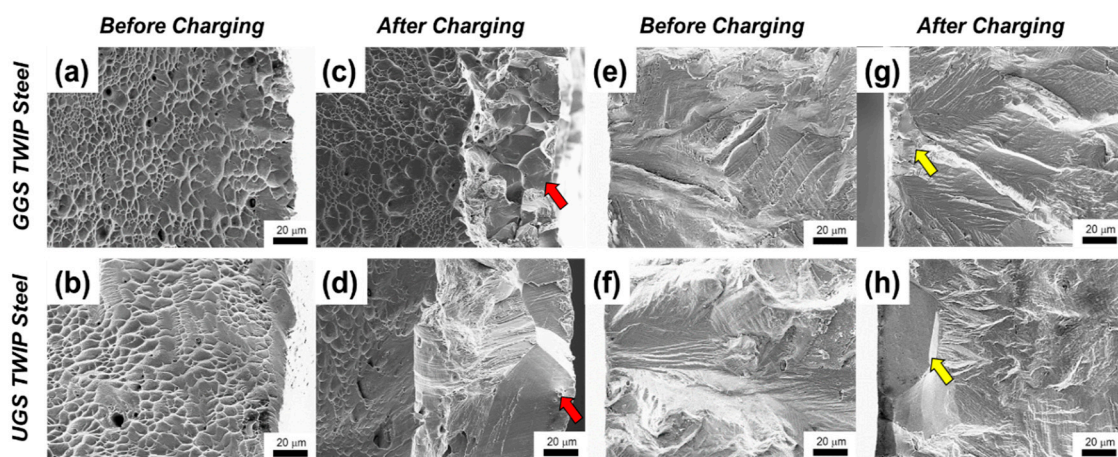


Figure 3. Fracture surface of the investigated materials in the (a–d) monotonic and (e–h) cyclic deformation modes. The images were obtained (a,b,e,f) before and (c,d,g,h) after hydrogen charging at a current density of $30 \text{ A}\cdot\text{m}^{-2}$ for 6 h at 360 K.

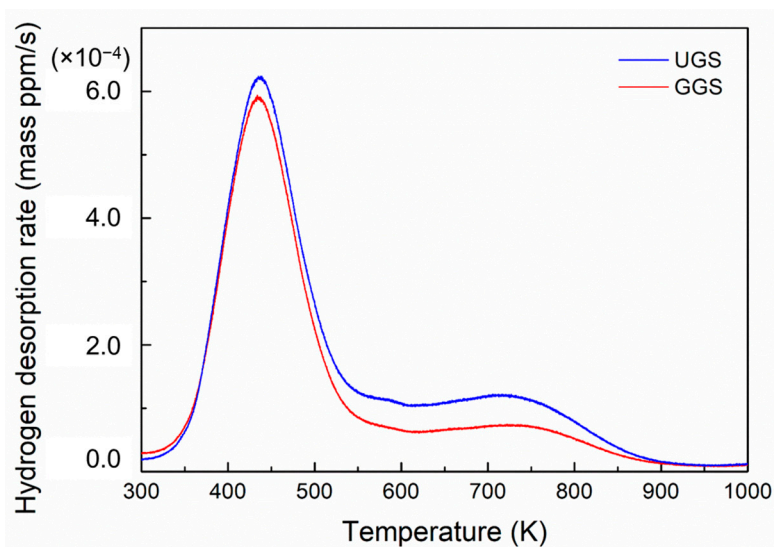


Figure 4. TDA spectra of the investigated steels after hydrogen charging at a current density of $30 \text{ A}\cdot\text{m}^{-2}$ for 6 h at 360 K.

The surface layer in GGS steel gave rise to the suppressed initiation of fatigue cracks as well as the improvement in HE resistance due to their relatively finer grains as compared with those in the interior. However, these beneficial effects were irrelevant to the grain structure of the material interior. A fine-grained interior instead decreases the LCF resistance by accelerating the growth of fatigue cracks [14,15]. The novelty of the current approach was that a fine-grained area just as wide as the hydrogen-affected zone was induced in the steel, leaving the coarse-grained sample interior unchanged. Consequently, mechanical deterioration in the cyclic deformation mode that is typically shown in fine-grained steels was successfully avoided in the GGS TWIP steel.

4. Conclusions

This study developed and inspected GGS TWIP steel with the bimodal grain structure. The grain size of surface layer (15.6 μm) was significantly finer than that of material interior (74.6 μm). The former accounted for a low volume fraction, thereby exerting a negligible influence on the mechanical properties in the monotonic deformation mode before hydrogen charging. Meanwhile, LCF resistance in the cyclic deformation mode was higher in GGS steel even before charging. It is particularly worth noting that GGS steel exhibited an obvious improvement in the HE resistance in both deformation modes as compared with the conventional UGS steel. The relatively fine-grained surface layer of GGS steel inhibited hydrogen penetration and reduced the density of hydrogen-enriched sites, resulting in a decrease in diffusible hydrogen content as compared to UGS steel. This result was consistent with the narrower area of the hydrogen-affected zone and the lower TDA spectrum confirmed in GGS steel. Moreover, the present approach avoided the fatigue deterioration caused by grain refinement by forming a relatively fine-grained area just as wide as the hydrogen-affected zone and leaving the coarse-grained interior unaffected.

Author Contributions: Conceptualization, S.W.S., T.L., and C.S.L.; investigation, S.W.S. and T.L.; resources, C.S.L.; writing—original draft preparation, S.W.S. and T.L.; writing—review and editing, T.L. and C.S.L.; supervision, C.S.L. All authors have read and agreed to the published version of the manuscript.

Funding: This work was supported by the National Research Foundation of Korea (NRF) grant funded by the Korean government (Ministry of Science and ICT) (No. 2018R1C1B6002068 & 2020R1A4A3079417).

Conflicts of Interest: The authors declare no conflict of interest.

References

1. Bouaziz, O.; Allain, S.; Scott, C.P.; Cugy, P.; Barbier, D. High manganese austenitic twinning induced plasticity steels: A review of the microstructure properties relationships. *Curr. Opin. Solid State Mater. Sci.* **2011**, *15*, 141–168. [[CrossRef](#)]
2. Koyama, M.; Akiyama, E.; Tsuzaki, K. Effect of hydrogen content on the embrittlement in a Fe–Mn–C twinning-induced plasticity steel. *Corros. Sci.* **2012**, *59*, 277–281. [[CrossRef](#)]
3. Allam, T.; Guo, X.; Sevsek, S.; Lipińska-Chwałek, M.; Hamada, A.; Ahmed, E.; Bleck, W. Development of a Cr–Ni–V–N Medium Manganese Steel with Balanced Mechanical and Corrosion Properties. *Metals* **2019**, *9*, 705. [[CrossRef](#)]
4. Koyama, M.; Akiyama, E.; Tsuzaki, K. Hydrogen embrittlement in a Fe–Mn–C ternary twinning-induced plasticity steel. *Corros. Sci.* **2012**, *54*, 1–4. [[CrossRef](#)]
5. Kim, D.; Jang, G.H.; Lee, T.; Lee, C.S. Orientation Dependence on Plastic Flow Behavior of Hydrogen-Precharged Micropillars of High-Mn Steel. *Met. Mater. Int.* **2020**, *26*, 1741–1748. [[CrossRef](#)]
6. Dieudonné, T.; Marchetti, L.; Wery, M.; Chêne, J.; Allely, C.; Cugy, P.; Scott, C.P. Role of copper and aluminum additions on the hydrogen embrittlement susceptibility of austenitic Fe–Mn–C TWIP steels. *Corros. Sci.* **2014**, *82*, 218–226. [[CrossRef](#)]
7. Song, S.W.; Kwon, Y.J.; Lee, T.; Lee, C.S. Effect of Al addition on low-cycle fatigue properties of hydrogen-charged high-Mn TWIP steels. *Mater. Sci. Eng. A* **2016**, *677*, 421–430. [[CrossRef](#)]
8. Kwon, Y.J.; Lee, T.; Lee, J.; Chun, Y.S.; Lee, C.S. Role of Cu on hydrogen embrittlement behavior in Fe–Mn–C–Cu TWIP steel. *Int. J. Hydrog. Energy* **2015**, *40*, 7409–7419. [[CrossRef](#)]

9. Chun, Y.S.; Park, K.-T.; Lee, C.S. Delayed static failure of twinning-induced plasticity steels. *Scr. Mater.* **2012**, *66*, 960–965. [[CrossRef](#)]
10. Allam, T.; Guo, X.; Lipińska-Chwałek, M.; Hamada, A.; Ahmed, E.; Bleck, W. Impact of precipitates on the hydrogen embrittlement behavior of a V-alloyed medium-manganese austenitic stainless steel. *J. Mater. Res. Technol.* **2020**, *9*, 13524–13538. [[CrossRef](#)]
11. Takahashi, J.; Kawakami, K.; Kobayashi, Y. Origin of hydrogen trapping site in vanadium carbide precipitation strengthening steel. *Acta Mater.* **2018**, *153*, 193–204. [[CrossRef](#)]
12. Zan, N.; Ding, H.; Guo, X.; Tang, Z.; Bleck, W. Effects of grain size on hydrogen embrittlement in a Fe-22Mn-0.6C TWIP steel. *Int. J. Hydrog. Energy* **2015**, *40*, 10687–10696. [[CrossRef](#)]
13. Park, I.J.; Lee, S.M.; Jeon, H.H.; Lee, Y.K. The advantage of grain refinement in the hydrogen embrittlement of Fe-18Mn-0.6C twinning-induced plasticity steel. *Corros. Sci.* **2015**, *93*, 63–69. [[CrossRef](#)]
14. Rusing, C.J.; Niendorf, T.; Frehn, A.; Maier, H.J. Low-Cycle Fatigue Behavior of TWIP Steel—Effect of Grain Size. *Adv. Mater. Res.* **2014**, *891*, 1603–1608. [[CrossRef](#)]
15. Ma, P.; Qian, L.; Meng, J.; Liu, S.; Zhang, F. Fatigue crack growth behavior of a coarse- and a fine-grained high manganese austenitic twin-induced plasticity steel. *Mater. Sci. Eng. A* **2014**, *605*, 160–166. [[CrossRef](#)]
16. Figueiredo, R.B.; Cetlin, P.R.; Langdon, T.G. The processing of difficult-to-work alloys by ECAP with an emphasis on magnesium alloys. *Acta Mater.* **2007**, *55*, 4769–4779. [[CrossRef](#)]
17. Lee, T.; Kwak, B.J.; Kong, T.; Lee, J.H.; Lee, S.W.; Park, S.H. Enhanced yield symmetry and strength-ductility balance of caliber-rolled Mg–6Zn–0.5Zr with ultrafine-grained structure and bulk dimension. *J. Alloy. Compd.* **2019**, *803*, 434–441. [[CrossRef](#)]
18. Koyama, M.; Sawaguchi, T.; Lee, T.; Lee, C.S.; Tsuzaki, K. Work hardening associated with epsilon-martensitic transformation, deformation twinning and dynamic strain aging in Fe-17Mn-0.6C and Fe-17Mn-0.8C TWIP steels. *Mater. Sci. Eng. A* **2011**, *528*, 7310–7316. [[CrossRef](#)]
19. De las Cuevas, F.; Reis, M.; Ferraiuolo, A.; Pratolongo, G.; Karjalainen, L.P.; Alkorta, J.; Gil Sevillano, J. Hall-Petch Relationship of a TWIP Steel. *Key Eng. Mater.* **2010**, *423*, 147–152. [[CrossRef](#)]
20. Shao, C.W.; Zhang, P.; Zhu, Y.K.; Zhang, Z.J.; Pang, J.C.; Zhang, Z.F. Improvement of low-cycle fatigue resistance in TWIP steel by regulating the grain size and distribution. *Acta Mater.* **2017**, *134*, 128–142. [[CrossRef](#)]
21. Han, D.K.; Lee, S.K.; Noh, S.J.; Kim, S.-K.; Suh, D.-W. Effect of aluminium on hydrogen permeation of high-manganese twinning-induced plasticity steel. *Scr. Mater.* **2015**, *99*, 45–48. [[CrossRef](#)]
22. Chou, S.-L.; Tsai, W.-T. Effect of grain size on the hydrogen-assisted cracking in duplex stainless steels. *Mater. Sci. Eng. A* **1999**, *270*, 219–224. [[CrossRef](#)]

Publisher’s Note: MDPI stays neutral with regard to jurisdictional claims in published maps and institutional affiliations.



© 2020 by the authors. Licensee MDPI, Basel, Switzerland. This article is an open access article distributed under the terms and conditions of the Creative Commons Attribution (CC BY) license (<http://creativecommons.org/licenses/by/4.0/>).